Supporting Information

Probing the metal/oxide interface of $IrCoCeO_x$ in the $N_2H_4 \cdot H_2O$ decomposition : an experimental and computational study

Silvio Bellomi[a], Daniel C. Cano-Blanco[b,c] , Ilaria Barlocco[a], Juan J. Delgado[d], Xiaowei Chen[d], Laura Prati[a], Davide Ferri[b], Nikolaos Dimitratos[e,f], Alberto Roldan[g], Alberto Villa[a]**

[a] Dipartimento di Chimica, Università degli Studi di Milano, via Golgi 19, I-20133, Milano, Italy

[b] Paul Scherrer Institut, PSI Center for Energy and Environmental Sciences, CH-5232, Villigen PSI, Switzerland

[c] École polytechnique fédérale de Lausanne (EPFL), Lausanne, Switzerland

[d] Departamento de Ciencia de los Materiales, Ingeniería Metalúrgica y Química Inorgánica, Facultad de Ciencias, Universidad de Cádiz, Campus Río San Pedro, Puerto Real (Cádiz) E-11510, Spain

[e] Dipartimento di Chimica Industriale "Toso Montanari", Alma Mater Studiorum Università di Bologna, Viale Risorgimento 4, Bologna 40126, Italy

[f] Center for Chemical Catalysis-C3, Alma Mater Studiorum Università di Bologna, Viale Risorgimento 4, Bologna 40136, Italy

[g] Cardiff Catalysis Institute, School of Chemistry, Cardiff University, Main Building, Park Place, CF10 3AT, Cardiff, United Kingdom

*Corresponding author:

E-mail addresses: alberto.villa@unimi.it, roldanmartineza@cardiff.ac.uk

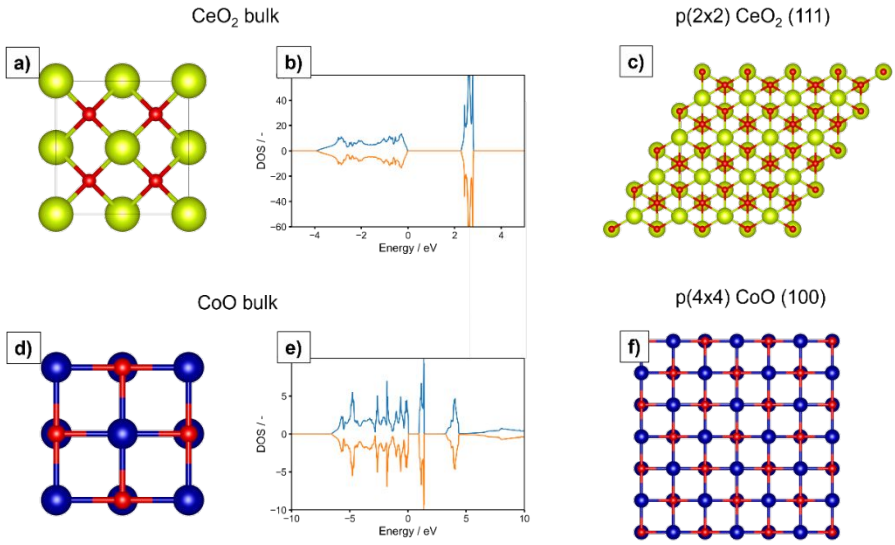

Figure S1 Bulk structure, Density Of States (DOS) and exposed crystal plane used in the slab calculations for CeO_2 (a, b and c), and CoO (d, e and f). For CoO, the DOS presented is relative to the Anti Ferro Magnetic II configuration (AFM II) to highlight the bandgap, thus the validity of the employed Hubbard parameters.

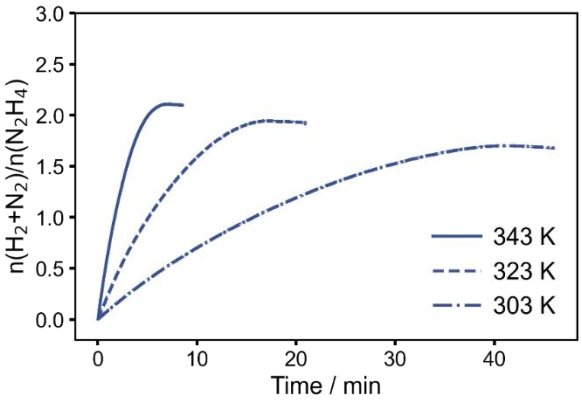

Figure S2 Kinetic profiles for the batch $N_2H_4{\cdot}H_2O$ decomposition reaction at different temperatures. All the experiments were performed at 1400 rpm, with 300 µL of a 3.3 M hydrous hydrazine solution in 5 mL of 0.5 M NaOH and an $N_2H_4 \cdot H_2O$: Ir molar ratio of 1000:1.

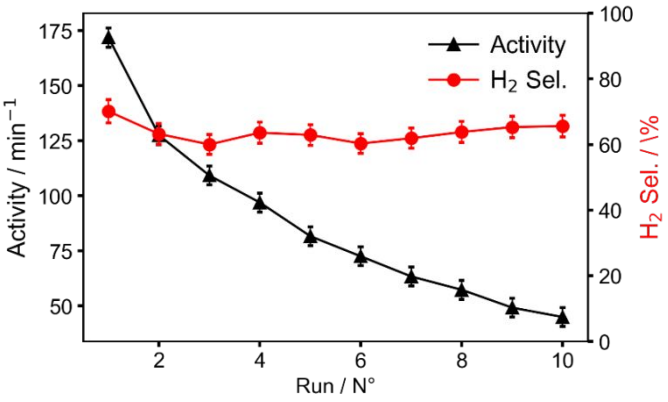

Figure S3 Stability trends for the $IrCoCeO_x$ catalyst in terms of activity, calculated with respect to 1 wt% Ir, and H_2 selectivity.

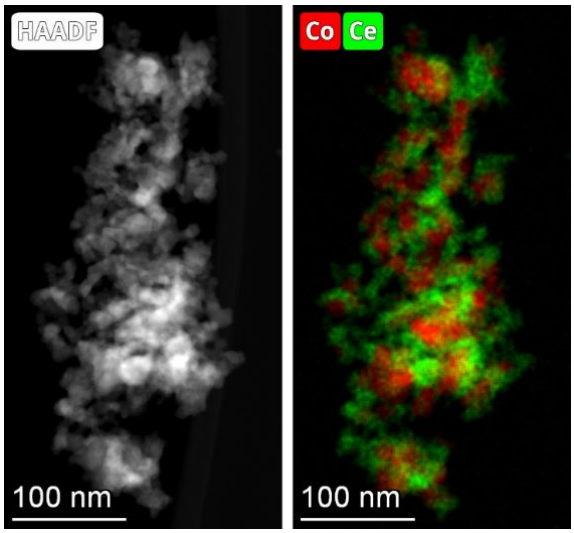

Figure S4 STEM-HAADF image of $CoCeO_x$ with corresponding XEDS mapping for Co and Ce.

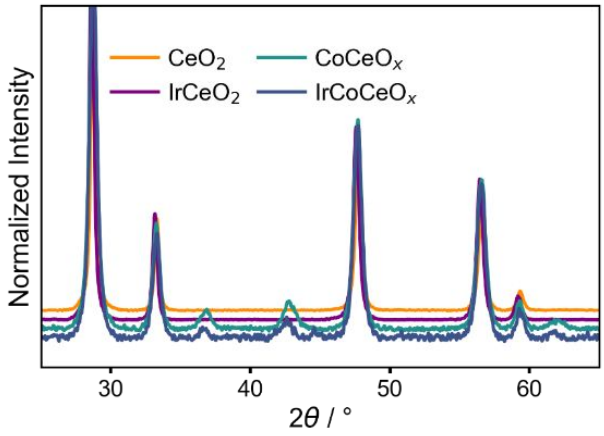

Figure S5 XRD patterns of the catalyst highlighting that the Ir introduction did not introduce any significant modification in the catalyst structure.

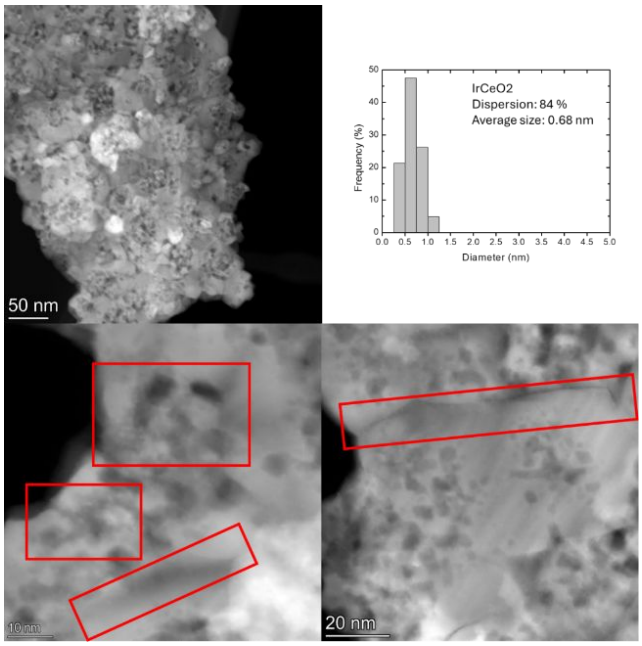

Figure S6 STEM-HAADF images of $IrCeO_2$ and particle size distribution showing sub-nanometric Ir species interacting with holes and irregularities of the support

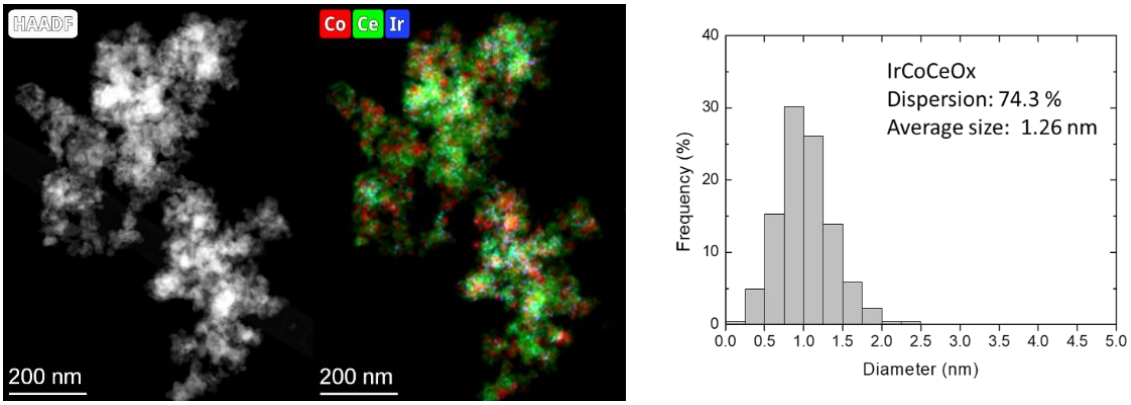

Figure S7 STEM-HAADF image of $IrCoCeO_x$ with corresponding XEDS mapping for Co, Ce and Ir and corresponding particle size distribution as obtained for Ir.

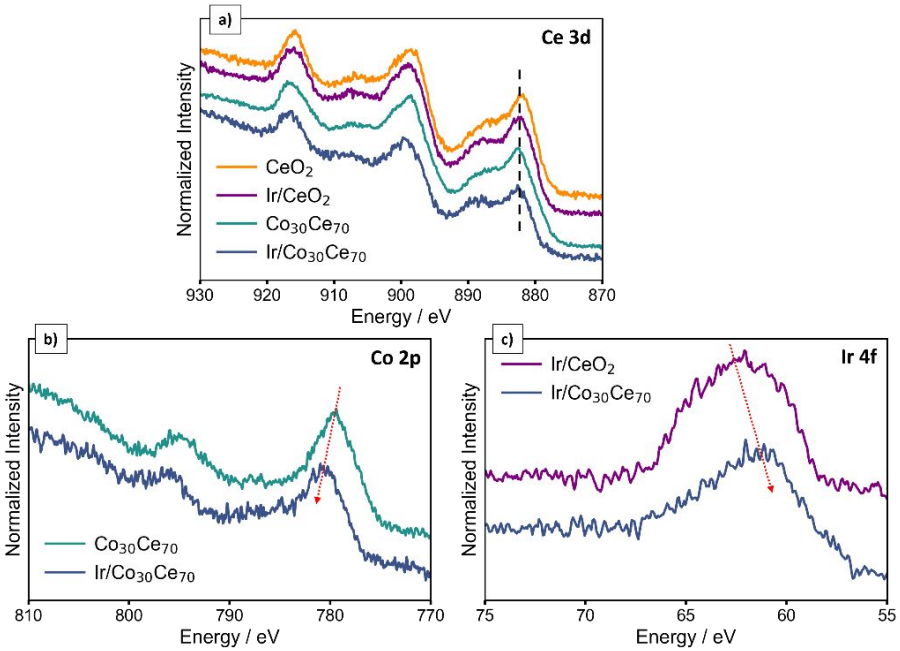

Figure S8 HR-XPS for the catalysts of the a) Ce 3d, b) Co 2p and c) Ir 4f edge.

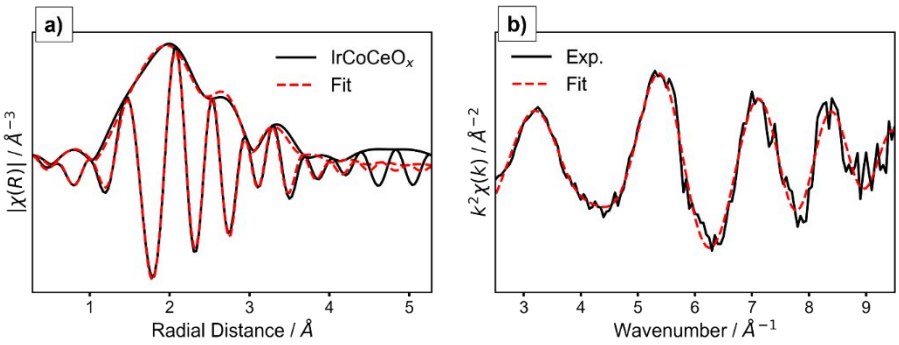

Figure S9 XAFS analysis for $IrCoCeO_x$. Best a) k^2-weighted FT-EXAFS and b) EXAFS fittings.

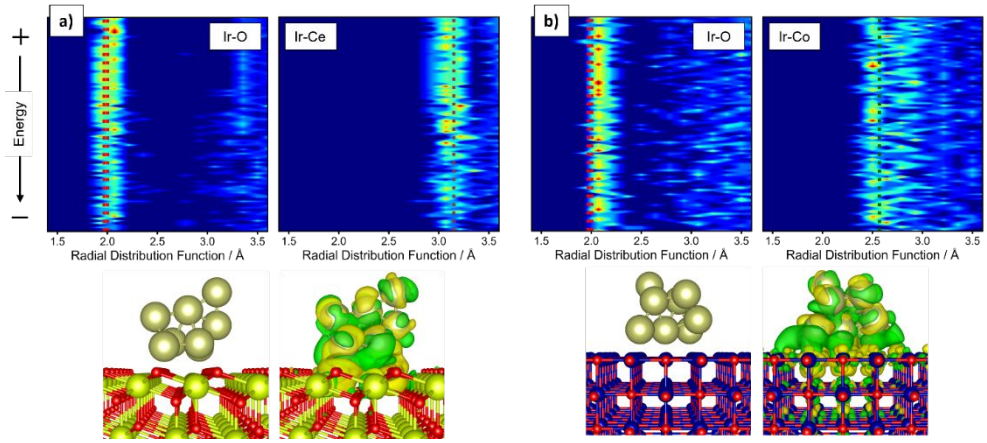

Figure S10 Stochastic search of supported cluster morphologies a) Ir_8/CeO_2 (111) and b) Ir_8/CoO (100). Radial Distribution Function evolution of Ir with the slabs atomic components (Ce and O for CeO_2, and Co and O for CoO) for the last 200 structures of the stochastic search, and putative global minima at frozen support geometry, with corresponding charge density difference plot (CDDP) after cluster adsorption. Yellow and green iso-surfaces denote gain and depletion of electron density respectively, i.e., accumulation of positive and negative charge, and the iso-surface value is 2×10^{-3} e$^-$ Å^{-2}. Insets in the RDF evolution plots are the bond distances as obtained from the CIF files of reference structures (IrO_2, Ir-Ce and Ir-Co intermetallic compounds).

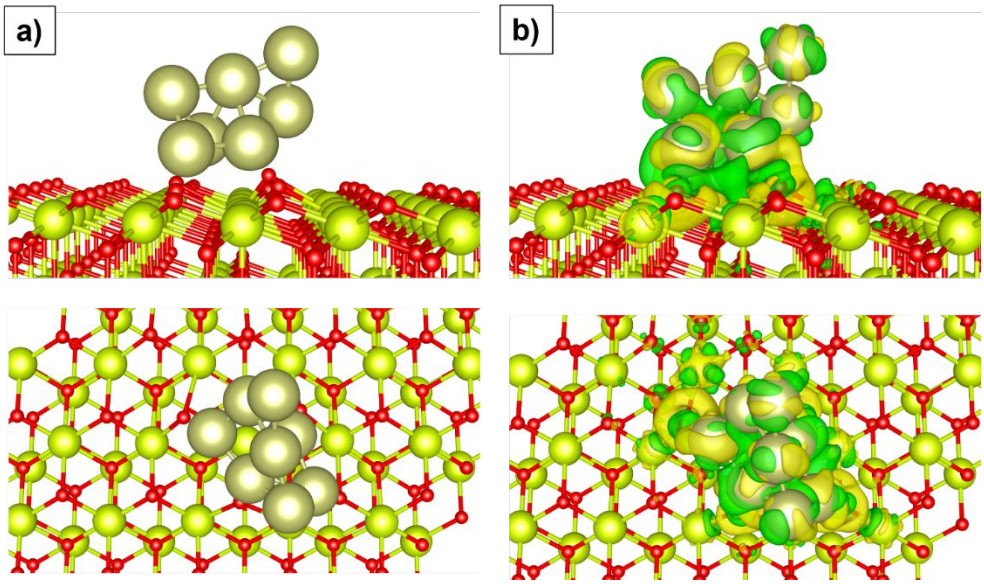

Figure S11 Interaction of Ir with CeO_2. Top and side view of the a) most stable Ir_8 geometry on CeO_2 (111) and b) corresponding charge density difference plot (CDDP) after cluster adsorption. Yellow and green iso-surfaces denote gain and depletion of electron density respectively, i.e., accumulation of positive and negative charge, and the iso-surface value is 2×10^{-3} e^- $Å^{-2}$.

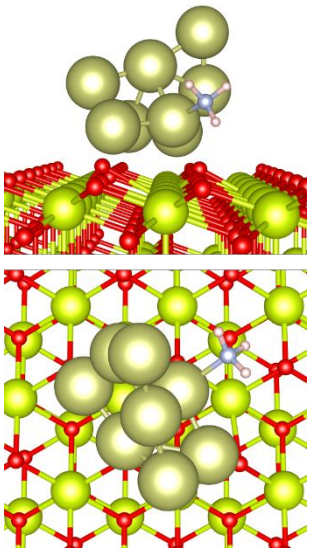

Figure S12 Top and side view for the most stable adsorption configuration of the probe molecule on Ir_8/CeO_2 (111).

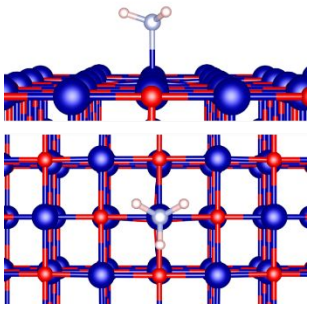

Figure S13 Most stable adsorption configuration of the probe molecule on CoO (100).

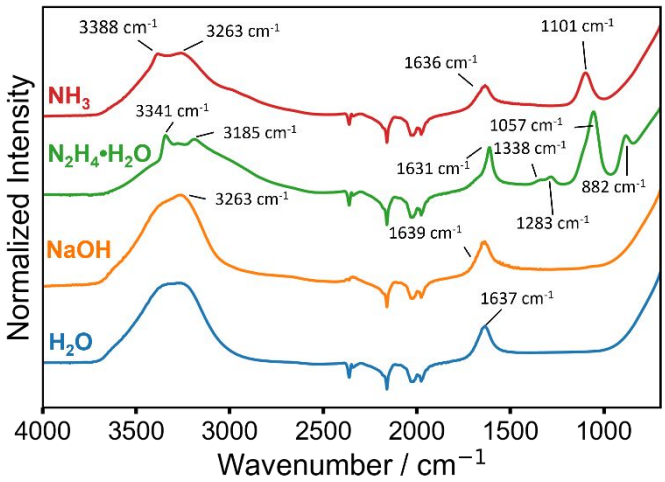

Figure S14 Ex-situ FT-IR spectra of the main reactants employed in the ME-ATR-IR experiments.

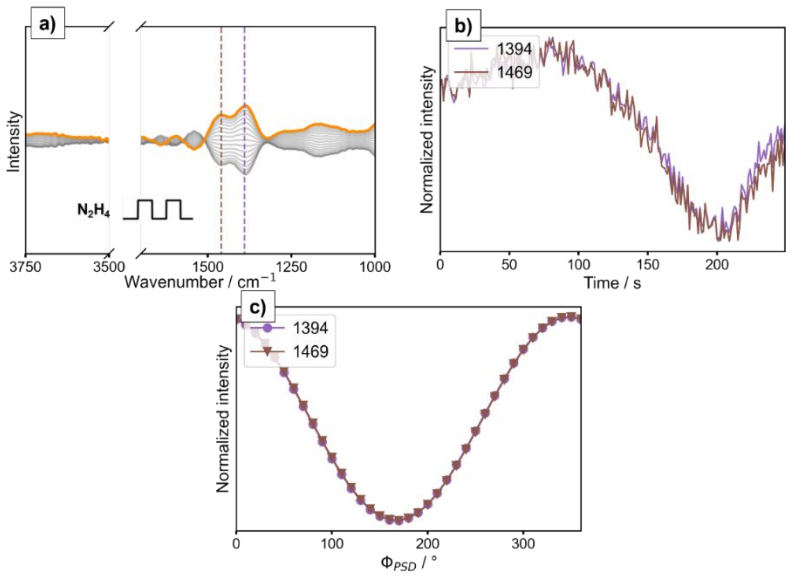

Figure S15 ME ATR-IR experiment of $N_2H_4 \cdot H_2O$ pulses in water on $IrCoCeO_x$. a) Phase-resolved ATR-IR spectra, b) time and c) phase evolution of the peaks labelled in a).

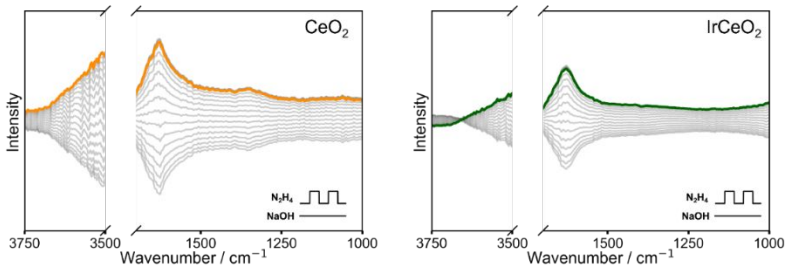

Figure S16 ME ATR-IR experiment of $N_2H_4 \cdot H_2O$ pulses in NaOH solutions for CeO_2 (left panel) and $IrCeO_2$ (right panel).

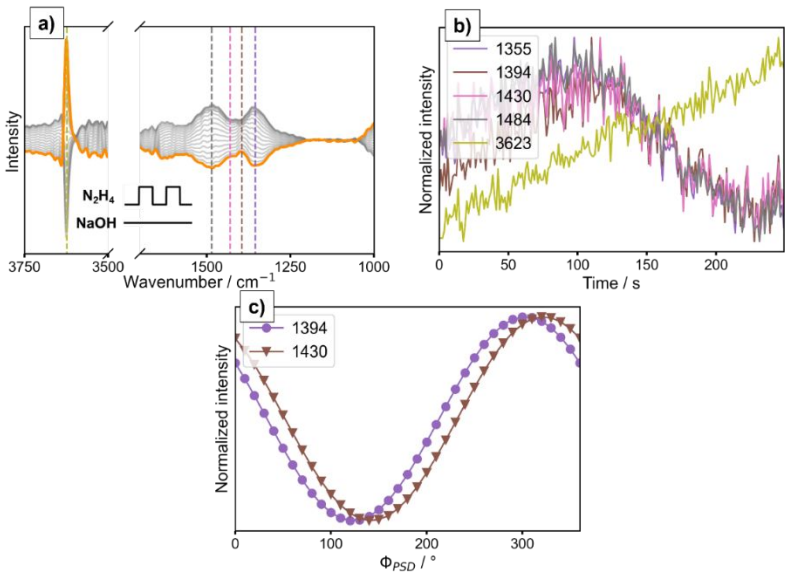

Figure S17 ME ATR-IR experiment of $N_2H_4 \cdot H_2O$ pulses in aqueous NaOH solution on $IrCoCeO_x$. a) Phase-resolved ATR-IR spectra, b) time and c) phase evolution of the peaks highlighted in a).

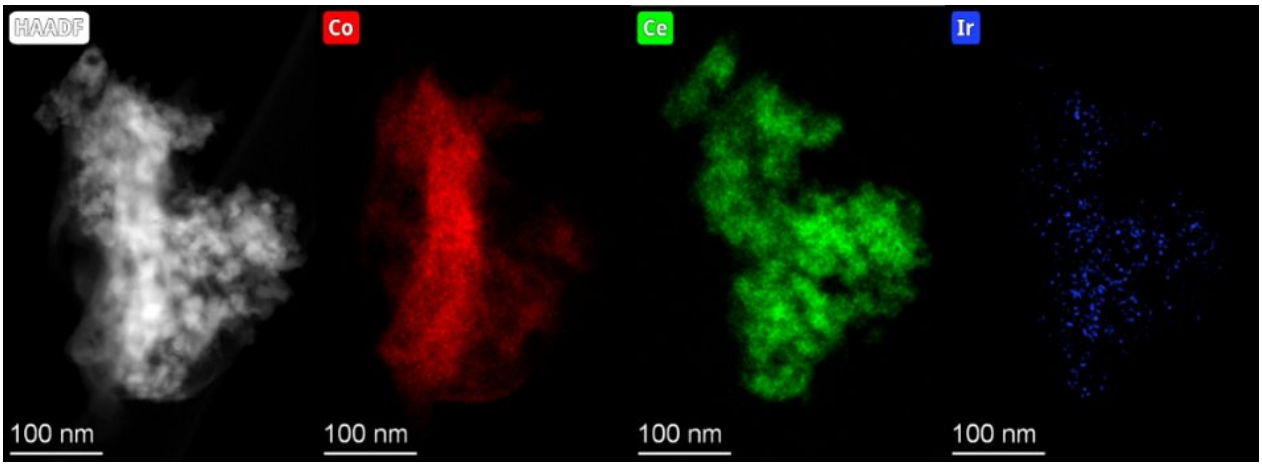

Figure S18 STEM-HAADF image of spent $IrCoCeO_x$ with corresponding XEDS mapping for Co, Ce and Ir.

Table S1 Structural parameters of the optimized bulk structures for CeO_2 and CoO.

Structure	a / Å	b / Å	γ / °
CeO_2	5.477	5.477	90.0
CoO	4.254	4.254	90.0

Table S2 Catalytic activities of different bimetallic supported catalysts used in hydrazine hydrate decomposition reaction.

Catalyst	TOF (h^{-1})	H_2 selectivity (%)	Solvent	T (K)	Ref
IrCoCeOx	2029	68	Aqueous NaOH	343	This work
$Rh_{4.4}Ni$@graphene	28	100	Aqueous NaOH	323	[1]
$Rh_{0.8}Ni_{0.2}$/MXene	857	100	Aqueous NaOH	323	[2]
$Ni_{85}Ir_{15}$@MIL-101	464	100	Aqueous NaOH	323	[3]
$Ni_{91}Ir_9/CeO_2$	97	100	Aqueous NaOH	323	[4]
Pd_3Ni/rGO	8400	100	Aqueous NaOH	323	[5]
$Ni_{0.8}Pt_{0.2}$/MIL-101-NH_2	137	100	Aqueous NaOH	303	[6]
Ni_5Pt_5-CeO_2	416	100	Aqueous NaOH	303	[7]
$Ni_{0.8}Pt_{0.2}$/DT-$T_3C_2T_x$	1220	100	Aqueous NaOH	323	[8]
Ni_3Fe-$(CeO_x)_{0.15}$/rGO	126	100	Aqueous NaOH	343	[9]
NiRh/V_2C	987	100	Aqueous NaOH	323	[11]
Ni_1Pt_1-ZrO_2	296	100	Water	303	[12]
Ni/TiO_2	265	100	Aqueous NaOH	343	[13]
Ni_4Pt/CeO_2	515	100	Aqueous NaOH	323	[14]

$Ni_{10}MoCo_x$/Mo–Ni–O	461	100	Aqueous NaOH	343	[15]

Table S3 Surface composition of the catalysts from the XPS survey scans.

	O 1s (at.%)	Ce 3d (at.%)	Co 2p (at.%)	Ir 4f (at.%)	C 1s (at.%)
CeO_2	41.51	8.42	/	/	50.07
$IrCeO_2$	33.24	6.81	/	0.52	59.42
$CoCeO_x$	30.95	6.65	6.44	/	55.96
$IrCoCeO_x$	42.21	4.29	2.45	0.83	54.33

Table S4 Summary of the EXAFS best fit parameters for the $IrCoCeO_x$ catalyst. For each scattering path, R denotes the path length, N defines the coordination number, ΔE0 is the energy-shift and σ2 is the Debye-Waller factor.

Scattering path	R	N	ΔE_0	σ^2
Ir-Ir	2.72 ± 0.01	2.3 ± 0.4	-2.7 ± 1.6	0.0069 ± 0.0002
Ir-O	1.96 ± 0.02	1.4 ± 0.1	-2.7 ± 1.6	0.0118 ± 0.0005
Ir-Co	2.58 ± 0.01	2.5 ± 0.3	-2.7 ± 1.6	0.0069 ± 0.0002

Table S5 Adsorption energies for the most stable configurations of the probe molecule for each slab model, metal-nitrogen (d(M-N)), average (d(N-H)) nitrogen-hydrogen, longest nitrogen-hydrogen (max(N-H)) bond-distances, spin multiplicity (Spin) and Bader charges of the metal-nitrogen couple..

	E_{ads} (E_{rec}) / eV	d (M-N) / Å	d (N-H) / Å	Max (N-H) / Å	Spin		q / |e|	
					M	N	M	N
Ir_8/CeO_2 (111)	-0.22	2.157	1.032	1.033	0	0	0.45	-1.22
CoO (100)	-2.53 (-0.57)	2.086	1.029	1.031	2	0	1.25	-1.25
Ir_8/CoO (100)	-5.50 (-2.82)	2.053	1.032	1.043	2	0	1.15	-1.25

References

(1) Wang, J.; Zhang, X.-B.; Wang, Z.-L.; Wang, L.-M.; Zhang, Y. Rhodium–Nickel Nanoparticles Grown on Graphene as Highly Efficient Catalyst for Complete Decomposition of Hydrous Hydrazine at Room Temperature for Chemical Hydrogen Storage. *Energy Environ Sci* **2012**, *5* (5), 6885. https://doi.org/10.1039/c2ee03344e.

(2) Liu, T.; Wang, Q.; Yuan, J.; Zhao, X.; Gao, G. Highly Dispersed Bimetallic Nanoparticles Supported on Titanium Carbides for Remarkable Hydrogen Release from Hydrous Hydrazine. *ChemCatChem* **2018**, *10* (10), 2200–2204. https://doi.org/10.1002/cctc.201701633.

(3) Zhao, P.; Cao, N.; Su, J.; Luo, W.; Cheng, G. NiIr Nanoparticles Immobilized on the Pores of MIL-101 as Highly Efficient Catalyst toward Hydrogen Generation from Hydrous Hydrazine. *ACS Sustain Chem Eng* **2015**, *3* (6), 1086–1093. https://doi.org/10.1021/acssuschemeng.5b00009.

(4) Dai, H.; Zhong, Y.; Wang, P. Hydrogen Generation from Decomposition of Hydrous Hydrazine over Ni-Ir/CeO2 Catalyst. *Progress in Natural Science: Materials International* **2017**, *27* (1), 121–125. https://doi.org/10.1016/j.pnsc.2016.12.012.

(5) Chen, Y.; Wang, L.; Zhai, Y.; Chen, H.; Dou, Y.; Li, J.; Zheng, H.; Cao, R. Pd-Ni Nanoparticles Supported on Reduced Graphene Oxides as Catalysts for Hydrogen Generation from Hydrazine. *RSC Adv* **2017**, *7* (51), 32310–32315. https://doi.org/10.1039/c7ra04390b.

(6) Liu, P.; Gu, X.; Wu, Y.; Cheng, J.; Su, H. Construction of Bimetallic Nanoparticles Immobilized by Porous Functionalized Metal-Organic Frameworks toward Remarkably Enhanced Catalytic Activity for the Room-Temperature Complete Conversion of Hydrous Hydrazine into Hydrogen. *Int J Hydrogen Energy* **2017**, *42* (30), 19096–19105. https://doi.org/10.1016/j.ijhydene.2017.06.191.

(7) Men, Y.; Su, J.; Wang, X.; Cai, P.; Cheng, G.; Luo, W. NiPt Nanoparticles Supported on CeO2 Nanospheres for Efficient Catalytic Hydrogen Generation from Alkaline Solution of Hydrazine. *Chinese Chemical Letters* **2019**, *30* (3), 634–637. https://doi.org/10.1016/j.cclet.2018.11.010.

(8) Guo, F.; Zou, H.; Yao, Q.; Huang, B.; Lu, Z. H. Monodispersed Bimetallic Nanoparticles Anchored on TiO2-Decorated Titanium Carbide MXene for Efficient Hydrogen Production from Hydrazine in Aqueous Solution. *Renew Energy* **2020**, *155*, 1293–1301. https://doi.org/10.1016/j.renene.2020.04.047.

(9) Men, Y.; Du, X.; Cheng, G.; Luo, W. CeOx-Modified NiFe Nanodendrits Grown on RGO for Efficient Catalytic Hydrogen Generation from Alkaline Solution of Hydrazine. *Int J Hydrogen Energy* **2017**, *42* (44), 27165–27173. https://doi.org/10.1016/j.ijhydene.2017.08.214.

(10) Wu, D.; Wen, M.; Gu, C.; Wu, Q. 2D NiFe/CeO2 Basic-Site-Enhanced Catalyst via in-Situ Topotactic Reduction for Selectively Catalyzing the H2 Generation from N2H4·H2O. *ACS Appl Mater Interfaces* **2017**, *9* (19), 16103–16108. https://doi.org/10.1021/acsami.7b00652.

(11) Tang, S.; Zhang, Z.; Xu, L.; Qin, H.; Dong, J.; Lv, Q.; Han, J.; Song, F. Ultrafine Nickel-Rhodium Nanoparticles Anchored on Two-Dimensional Vanadium Carbide for High Performance Hydrous Hydrazine Decomposition at Mild Conditions. *J Colloid Interface Sci* **2024**, *669*, 228–235. https://doi.org/10.1016/j.jcis.2024.04.204.

(12) Hussain, S. N.; Raza, N.; Alomar, T. S.; AlMasoud, N.; Gul, H.; Ashraf, G.; Ansari, M. Z.; Yasin, G. NiPt Nanoparticle Immobilization on Zirconia (ZrO2) for the Production of Hydrogen through Selected Decomposition of Alkaline Hydrazine Solution. *Materials Science and Engineering: B* **2024**, *302*, 117267. https://doi.org/10.1016/j.mseb.2024.117267.

(13) Liu, Y.; Liu, X.; Liu, X.; Li, Y.; Ma, J.; Ma, C. TiO2 Nanoparticle-Supported Ni Catalyst for the Dehydrogenation of Hydrazine Hydrate. *Chemosphere* **2023**, *313*, 137608. https://doi.org/10.1016/j.chemosphere.2022.137608.

(14) Qiu, Y.-P.; Chen, M.-H.; Qin, S.-H.; Yang, Z.-Q.; Wang, P. Modulation of Metal/Support Interactions Improves Catalytic Performance of Ni–Pt/CeO2 for Hydrogen Generation from Hydrazine Monohydrate. *Int J Hydrogen Energy* **2024**, *50*, 1381–1390. https://doi.org/10.1016/j.ijhydene.2023.09.244.

(15) Qin, S.-H.; Qiu, Y.-P.; Chen, M.-H.; Wang, P. Noble-Metal-Free Ni 10 MoCo x /Mo–Ni–O as an Active and Durable Catalyst for Hydrogen Generation from Hydrazine Monohydrate. *J Mater Chem A Mater* **2023**, *11* (39), 21411–21419. https://doi.org/10.1039/D3TA04602H.